# EFFECT OF MISSING STRUT LOCATION ON THE STIFFNESS AND STRESS OF BCC LATTICE SPECIMENS UNDER COMPRESSION

**JOZEF TKAC[1], MARTIN KOROL[1], DOMINIK CUHA[1]**

[1]Technical University of Kosice, Faculty of Manufacturing Technologies with a seat in Presov, Slovakia

**DOI: 10.17973/MMSJ.2026_11_2026046**

**jozef.tkac@tuke.sk**

This paper numerically compares the axial stiffness and local stress of three BCC lattice specimens under compression. The intact REF model is compared with the INT and SIDE models, which have one missing internal strut and one missing strut near a lateral surface, respectively. All variants use the same linear elastic structural steel model, end plates, and prescribed axial displacement of 0.01 mm. Calculations were performed using nominal element sizes of 0.5 and 0.4 mm. Compared with REF, axial stiffness decreased by approximately 0.593% for INT and 0.276 – 0.282% for SIDE. The stiffness ranking remained unchanged for both meshes. The maximum local stress on the monitored retained strut was more sensitive to mesh size. For INT, the sign of the difference relative to REF also changed. The results demonstrate the need to evaluate the stiffness of the entire specimen and stress in the selected region separately.

**KEYWORDS**

BCC lattice structure, missing strut, defect location, finite element method, elastic stiffness, mesh sensitivity

## 1 INTRODUCTION

Lattice structures consist of repeating cells composed of interconnected struts. Their mechanical properties depend on the arrangement and dimensions of the struts, the material used, and the mode of loading [Bulej 2022]. Safka et al. compared a body-centered cubic (BCC) structure and a cross-type strut structure, both fabricated from PA12 polyamide using Multi Jet Fusion. Under uniaxial tension, the cross structure was stiffer at the same material volume fraction and build orientation, whereas the BCC structure exhibited greater displacement to failure [Safka 2020]. These results demonstrate the importance of strut arrangement and test conditions. However, values measured in tensile tests on polymer specimens cannot be directly applied to a steel BCC structure under compression. This study therefore compares three BCC variants using the same material model and loading.

Advances in metal additive manufacturing have expanded the possibilities for fabricating and investigating lattice structures. Maconachie et al. reviewed structures fabricated by selective laser melting (SLM). They summarized the relationships between cell arrangement, relative density, and mechanical properties [Maconachie 2019]. Hanks et al. compiled a database covering 18-unit cell topologies based on analytical, numerical, and experimental results [Hanks 2020]. These studies aid structure selection while also showing that the results depend on specimen dimensions, material, and manufacturing process. When assessing missing struts, it is therefore important to use a common baseline model and the same loading. In addition to the values themselves, their changes relative to the intact specimen should also be reported. Ushijima et al. derived relationships for initial stiffness and plastic collapse strength. They compared the results with beam and solid element models and with compression tests [Ushijima 2011]. Their work helps determine when a simpler beam model is sufficient and when a more detailed solid model of the joints is required. This choice also depends on the ratio of strut length to its cross-sectional dimensions. Moreover, when assessing a single missing strut, its surrounding region and the boundaries of the entire specimen must be captured. Model accuracy is also affected by the geometry of the joints and strut cross sections. Gumruk and Mines showed that material overlap at the joints affects the calculated initial stiffness and strength of stainless steel microlattice structures [Gumruk 2013]. Vrana et al. analyzed BCC structures fabricated by selective laser melting using micro-computed tomography. They subsequently used the measured strut dimensions in computational models. An elliptical cross section represented the actual strut shape and mechanical response better than a circular cross section [Vrana 2020]. Such deviations in shape and dimensions constitute a different type of defect from a completely missing strut. This study uses a three-dimensional solid model of CAD geometry from which a selected strut was deliberately removed. Dobrovszky et al. also used simulations and compression tests to investigate the influence of the outer shell of gyroid TPMS structures fabricated by stereolithography. The spatial arrangement of the gyroid had a greater influence on the results for specimens without a shell than for enclosed specimens [Dobrovszky 2024]. Their study involves a photopolymer and a different cell type. It is relevant to the present work because it demonstrates the importance of external load-bearing components when assessing the entire specimen. However, it does not directly explain the effect of a missing strut in BCC. Imperfections other than completely missing struts also occur during the manufacture of lattice structures. Echeta et al. classified dimensional inaccuracies, surface irregularities, and porosity in structures fabricated by powder bed fusion and described methods for measuring and mitigating them [Echeta 2020]. Several types of defects may occur simultaneously. Liu et al. used X-ray tomography and numerical models to investigate strut waviness, thickness variations, and oversizing relative to the design. They examined the effects of these defects on the elastic behavior and failure of metallic structures [Liu 2017]. Lozanovski et al. proposed a CAD procedure that represents variations in cross sections and the positions of their centroids based on measured geometry [Lozanovski 2019]. These methods allow a model to more closely represent an as-manufactured specimen. Complete removal of a strut from the CAD model is a simpler approach that allows this specific defect to be investigated independently [Bozek 2023].

Goodall et al. also investigated completely missing struts. In Ti6Al4V structures, they used these to simulate manufacturing defects and assessed damage and its distribution through experimental measurements of deformation [Goodall 2019]. Gross et al. compared four types of strut-based structures with missing elements. They found that the sensitivity of elastic properties to these defects depends on the arrangement of the underlying structure [Gross 2019]. Thus, in addition to the number of missing struts, their locations and the connectivity of the surrounding network also matter.

Comparing internal and lateral defects in a BCC specimen is therefore meaningful when the missing struts and their surroundings are precisely defined. The numerical and experimental study by Huang et al. on the sensitivity of BCC structures to defects is closely related to the topic of this paper [Huang 2024]. The authors investigated irregular cell arrangements, wavy and missing struts, and their effects on the

elastic modulus under compression and the initial yield strength. Investigating a missing strut is therefore not, in itself, a new topic. Bruson et al. subsequently combined X-ray computed tomography with image analysis and examined the combined effects of porosity and geometric irregularities in polymeric BCC structures [Bruson 2025]. Although they used a different material and different types of defects, this work also demonstrates the need to precisely describe the imperfection included in the computational model [Saga 2018]. The stiffness of the entire specimen and stress at individual joints need to be evaluated separately. Dallago et al. compared the results of quasi-static and fatigue tests with finite element calculations. They used both the designed CAD geometry and geometry obtained from tomography and demonstrated the importance of manufacturing imperfections in fatigue assessment [Dallago 2019]. Benedetti et al. reviewed the mechanical behavior of cellular materials with a designed internal architecture, focusing on design and manufacturing for fatigue resistance [Benedetti 2021]. These studies explain why local increases in stress are important for service life.

However, the result of a single elastic simulation does not, on its own, determine the collapse load, fatigue life, or energy absorbed during compression. Tkac et al. combined CAD modeling, finite element calculations, and compression tests on additively manufactured ABS structures [Tkac 2020]. They subsequently used industrial computed tomography to examine their surface and internal geometry [Tkac 2022]. These studies demonstrate the possibilities for experimentally validating structures and their dimensions. This study uses an idealized structural steel model. Previous ABS tests therefore do not serve to validate its material properties.

The aim of this paper is to compare an intact BCC specimen (REF), a specimen with one missing internal strut (INT), and a specimen with one missing strut near a lateral surface (SIDE). All variants have the same material model and prescribed displacement. The reaction force, stiffness of the entire specimen, and equivalent stress on a selected retained strut are compared. Calculations using two mesh sizes show how sensitive these quantities are to mesh refinement. The contribution lies in comparing two specific defect locations and assessing the reliability of the selected indicators.

## 2 MATERIAL AND METHODS

The geometric models of all three BCC lattice specimens were created in PTC Creo Parametric 13. They were then imported into Ansys Workbench 2026 R1, where finite element simulations of compressive loading were set up and performed using the Static Structural system and the Mechanical module. The same material model, boundary conditions, and evaluation procedure were used for the REF, INT, and SIDE variants.

### *2.1 Geometry and definition of defects*

The baseline CAD model has a BCC arrangement with a cell size of 8 mm and struts with a circular cross-section and a diameter of 1.6 mm. Four cells are repeated in each coordinate direction, giving external lattice dimensions of 32 × 32 × 32 mm. Both the upper and lower plates are 2 mm thick, and the total specimen height is 36 mm. The struts and plates form a single continuous solid body. The distance from the center to a corner of a cell is 6.928 mm. The free strut length is shorter because its ends overlap with adjacent struts at the joints.

The main specimen dimensions and the locations of the missing struts are shown in Figure 1. Dimensions A and B are 32 mm, and the total height (H) is 36 mm. The REF model in Figure 1 a) contains all struts. Copies of this model were used to create the SIDE variant in Figure 1 b) by removing one strut near the lateral surface and the INT variant in Figure 1 c) by removing one strut in the interior region. In Figure 1b and 1c, the removed strut is highlighted in red, and its location is marked with a circle. This depiction serves only to identify the defect. The strut is absent from the corresponding computational model. The plates and all other geometric parameters remained the same.

Here, one strut means the segment from the center to a corner of a cell between two adjacent joints. Two such segments form the complete body diagonal of the cell. Although one strut is missing in each variant, the volume of material removed may not be exactly the same. It is affected by strut overlap at the joints and by the trimming of the geometry at the specimen boundary.

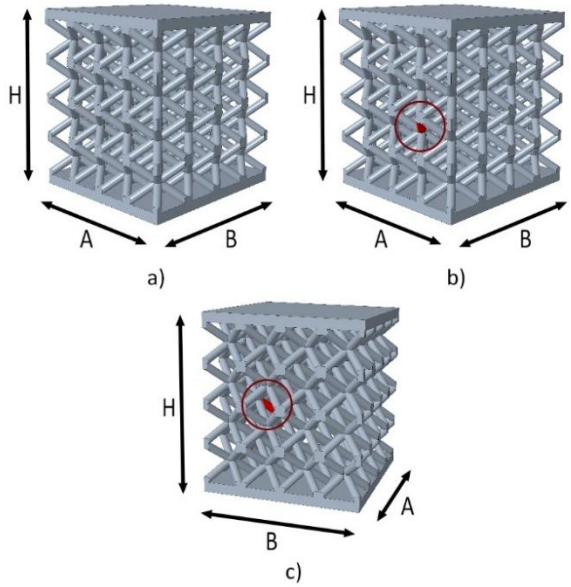



**Figure 1.** Geometry of the BCC lattice specimens – a) REF specimen, b) SIDE specimen, c) INT specimen

### *2.2 Material model and boundary conditions*

All three models were assigned the Structural Steel material from the Ansys Engineering Data library. The material model is isotropic and linearly elastic, meaning that it has the same elastic properties in all directions. Young's modulus is 200 000 MPa, Poisson's ratio is 0.30, and the density is 7 850 kg/m$^3$. The library also specifies a tensile and compressive yield strength of 250 MPa and an ultimate tensile strength of 460 MPa. However, the analysis includes only elastic deformation. These strength values do not, by themselves, activate plasticity or failure calculations. Thermal, electrical, magnetic, and fatigue data are not used in this static analysis. The main parameters are listed in Table 1.

| Parameter | Value |
|---|---|
| Strut diameter | 1.6 mm |
| Cell edge length | 8 mm |
| Core cell arrangement | 4 × 4 × 4 |
| External core dimensions | 32 × 32 × 32 mm |
| Plate thickness | 2 mm |
| Total height | 36 mm |
| Young's modulus E | 200 000 MPa |
| Poisson's ratio ν | 0.30 |
| Density ρ | 7 850 kg/m$^3$ |
| Prescribed displacement of the upper face | UY = − 0.01 mm |
| Nominal mesh sizes | 0.5 and 0.4 mm |

**Table 1.** Model dimensions, material properties, and loading settings

The specimen is compressed along the global Y-axis. The external bottom face of the lower plate is fixed in all displacement directions. A displacement of UY = −0.01 mm is prescribed on the external upper face. Displacements of the upper face in the X and Z directions remain free. The other surfaces are unloaded. Both the upper and lower plates are part of the elastic model and can deform. The bottom and upper faces therefore have different boundary conditions, but these conditions are the same for all three variants. A schematic of the loading and restraints is shown in Figure 2.

The calculation is set up as a linear static analysis with the large-deformation option disabled. A single load step is used, with an end time of 1 s. This time serves only as a load-step parameter and does not represent the duration of a physical test. No additional force, pressure, or gravity is applied. The reaction force is evaluated in the Y-axis direction on the upper face with the prescribed displacement.

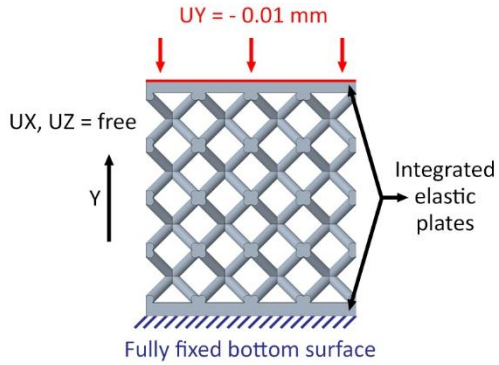



**Figure 2.** Schematic of the prescribed displacement along the Y-axis and fixed restraint of the bottom face

### 2.3 Computational mesh and solution checks

The computational mesh consists of ten-node quadratic tetrahedral SOLID187 elements. Two specified global element sizes, h = 0.5 mm and h = 0.4 mm, are compared using the same meshing procedure. At a size of 0.5 mm, the SIDE model has a total of 684 348 elements and 1 091 378 nodes. At a size of 0.4 mm, it has 1 136 622 elements and 1 788 748 nodes. The specified size controls mesh generation. Individual elements adapt to the geometry, so their edges do not all have the same length. The solver output for SIDE with the 0.4 mm mesh confirms that the PCG solver convergence criterion was satisfied, the load step was completed, and no error messages were recorded. The calculation on the specified mesh was therefore completed. However, this does not mean that further mesh refinement will leave the result unchanged.

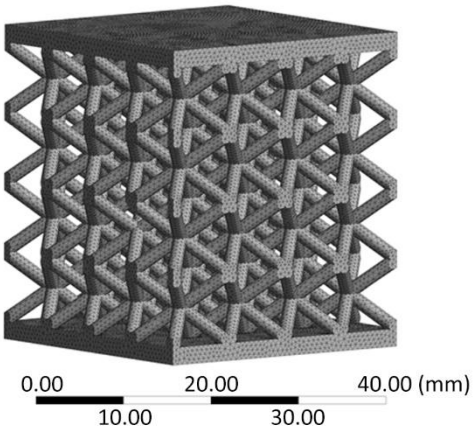



**Figure 3.** Computational mesh of the SIDE BCC lattice model

The comparison of two meshes shows the sensitivity of the results to mesh size. Additional calculations would be needed to reliably determine the convergence rate and estimate the value under further refinement. The computational mesh of the SIDE BCC lattice model is shown in Figure 3. The overall 3D view shows the mesh at a nominal element size of h = 0.4 mm.

The details in Figure 4 focus on a retained strut and its connections to adjacent struts. This strut was selected to compare local equivalent stress among the REF, SIDE, and INT models. Figure 4 a) shows the mesh of the SIDE specimen at h = 0.4 mm, and Figure 4 b) shows it at h = 0.5 mm. The identical orientation and magnification of the two details allow a direct comparison of the distribution and density of elements on the monitored strut and at its joints. The triangles visible on the model surface represent the surface faces of the solid tetrahedral elements. Individual element sizes adapt to the local geometry, so the specified h value does not imply that all mesh edges have the same length.

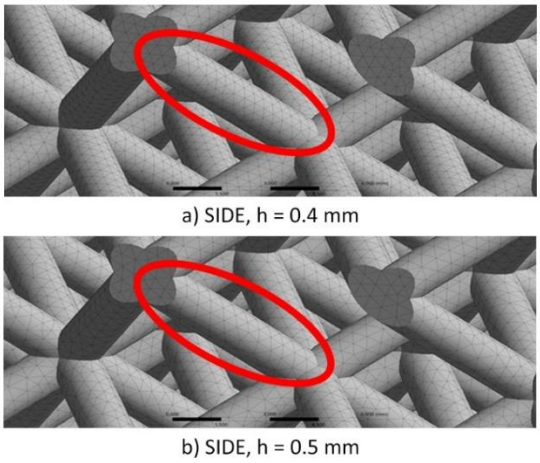



**Figure 4.** Computational mesh of the SIDE BCC lattice model – a) Detail at h = 0.4 mm, b) Detail at h = 0.5 mm

### 2.4 Evaluated quantities

The effect of a missing strut is evaluated using the axial stiffness of the specimen and von Mises equivalent stress. The results for the INT and SIDE variants are compared with the REF reference model under the same boundary conditions and at the same nominal element size. Axial stiffness expresses the resistance of the whole specimen, including the end plates, to compression. It is determined as the ratio of the magnitude of the reaction force in the Y-axis direction to the magnitude of the prescribed displacement of the upper plate:

$$K_i = \frac{|F_{Yi}|}{\delta} \quad (1)$$

where $K_i$ is the whole-specimen axial stiffness, including the end plates [N/mm], $F_{yi}$ is the absolute value of the reaction force of the corresponding specimen in the Y-axis direction [N], and δ is the magnitude of the prescribed displacement of the upper plate [mm]. Axial stiffness characterizes the whole specimen and depends on its geometry and restraint. Young's modulus used in the material model characterizes the elasticity of the steel. Relative stiffness is used to compare the variants with defects against the reference specimen:

$$R_i = \frac{|K_i|}{K_{REF}} \quad (2)$$

where $R_i$ is the dimensionless ratio of the stiffness of the model with a defect to the stiffness of the reference model, $K_i$ is the axial stiffness of the compared model INT or SIDE [N/mm], and $K_{REF}$ is the axial stiffness of the intact REF reference model [N/mm].

A value of $R_i$ = 1 indicates the same stiffness as that of the REF model. Values below 1 indicate lower stiffness, and values above 1 indicate higher stiffness. The percentage change in stiffness is calculated using the following expression:

$$\Delta K_i = 100.(R_i - 1)\ [\%] \quad (3)$$

where $\Delta K_i$ is the percentage change in the stiffness of the corresponding model relative to REF [%], $R_i$ is the relative stiffness calculated using the preceding equation, and the value 1 corresponds to the stiffness of the reference model. A negative result indicates a decrease in stiffness, and a positive result indicates an increase. For example, $\Delta K_i$ = -2% means that the specimen is 2% less stiff than the REF specimen. The compared stiffness values always refer to the same nominal element size.

Von Mises equivalent stress is evaluated throughout the solid body and separately on two selected surface faces of one retained strut. The overall maximum allows the region of the highest stress in the specimen to be identified. The local maximum and the Ansys-reported average stress are compared on the monitored strut. Stress values are reported in MPa. The monitored strut has the same position and orientation in all three models. It is marked with a red ellipse in Figure 4. However, its position relative to the missing strut differs between the INT and SIDE variants. The local results therefore describe the effect of defect location on this specific monitored region.

The "Averaged" setting is used to evaluate stress. The "Average" value denotes the Ansys-reported average for the selected surface faces. In this study, it is reported as a software output, without assuming that it represents an average weighted by the area or volume of the strut. The local maximum and the "Average" value are compared with the corresponding results of the REF model at the same mesh size.

The sensitivity of the results to mesh size is assessed by comparing the calculations at h = 0.5 mm and h = 0.4 mm. The percentage change in the monitored quantity after mesh refinement is determined using the following equation:

$$d_q = 100.\left(\frac{q_{0.4}}{q_{0.5}} - 1\right)\ [\%] \quad (4)$$

where $d_q$ is the percentage change in the monitored result after refining the mesh from 0.5 to 0.4 mm [%], $q_{0.4}$ is the value of the monitored quantity at a nominal element size of h = 0.4 mm, and $q_{0.5}$ is the value of the monitored quantity at a nominal element size of h = 0.5 mm.

Both q values always refer to the same model, the same quantity, and the same monitored region. A positive $d_q$ value indicates an increase in the result with the finer mesh, and a negative value indicates a decrease.

When interpreting the effect of the defect, whether the result is higher or lower than the corresponding REF result for both meshes is also considered. If it is higher with one mesh and lower with the other, the direction of its change cannot be reliably determined from the available calculations.

## 3 RESULTS

This section compares the results for the REF, INT, and SIDE models at the same prescribed axial displacement of 0.01 mm. The calculations are evaluated at nominal element sizes of 0.5 and 0.4 mm. The reaction force, axial stiffness of the entire specimen, and equivalent stress on the monitored retained strut are compared. Changes in the results following mesh refinement are also assessed.

### *3.1 Reaction force and specimen stiffness*

Table 2 presents the magnitudes of the reaction forces in the Y direction and the corresponding axial stiffnesses of the REF, INT, and SIDE models. The stiffnesses were calculated from the reaction forces and the prescribed displacement using the relationship given in Subsection 2.4. The effect of the missing strut is evaluated by comparing the INT and SIDE variants with the REF model at the same mesh size.

| Model | h [mm] | $\|F_Y\|$ [N] | K [N/mm] |
|---|---|---|---|
| REF | 0.5 | 772.52 | 77 252 |
| | 0.4 | 768.73 | 76 873 |
| INT | 0.5 | 767.94 | 76 794 |
| | 0.4 | 764.17 | 76 417 |
| SIDE | 0.5 | 770.34 | 77 034 |
| | 0.4 | 766.61 | 76 661 |

Table 2. Reaction force and axial stiffness of the entire specimen

At both mesh sizes, the REF model has the highest stiffness, followed by SIDE, while INT has the lowest stiffness. Compared with REF, the stiffness of INT is lower by 0.593% at h = 0.5 mm and by 0.593% at h = 0.4 mm. For SIDE, the reduction in stiffness is 0.282% at h = 0.5 mm and 0.276% at h = 0.4 mm. At the finer mesh, the relative stiffnesses are approximately $R_{INT}$ = 0.9941 and $R_{SIDE}$ = 0.9972. The stiffness ranking and the signs of the differences relative to REF remain the same for both meshes.

### *3.2 Local equivalent stress on the monitored strut*

Table 3 summarizes the von Mises equivalent stress evaluated on two selected surface faces of the monitored retained strut. At h = 0.4 mm, the local maxima are 60.959 MPa for the REF specimen, 59.174 MPa for the INT specimen, and 65.925 MPa for the SIDE specimen. The corresponding Ansys-reported averages are 14.274 MPa, 14.164 MPa, and 14.798 MPa. These values describe the selected local region.

| Model | h [mm] | Maximum [MPa] | Average [MPa] |
|---|---|---|---|
| REF | 0.5 | 50.812 | 14.527 |
| | 0.4 | 60.959 | 14.274 |
| INT | 0.5 | 55.378 | 14.548 |
| | 0.4 | 59.174 | 14.164 |
| SIDE | 0.5 | 59.382 | 14.956 |
| | 0.4 | 65.925 | 14.798 |

Table 3. Equivalent stress on selected surface faces of the monitored strut

Compared with REF at the same mesh size, the local maximum in SIDE is higher by 16.87% at h = 0.5 mm and by 8.15% at h = 0.4 mm. For INT, the maximum at h = 0.5 mm is higher by 8.99%, but at h = 0.4 mm it is lower by 2.93%. The sign of the difference between INT and REF therefore depends on the mesh used.

The Ansys-reported average for SIDE is higher than that for REF by 2.95% at h = 0.5 mm and by 3.67% at h = 0.4 mm. For INT, it remains close to the reference value. The changes are +0.14% and −0.77%. A comparison of the local maxima and reported averages for both meshes is shown in Figure 5. The lines in the graph only connect the results for the two meshes and do not predict the trend with further refinement.

### *3.3 Mesh size effects and stress distribution*

Following mesh refinement from 0.5 to 0.4 mm, the reaction force and axial stiffness changed by −0.491% for the REF specimen, by −0.491% for INT, and by −0.484% for SIDE. The changes are similar for all three models, and their magnitudes are less than 0.5%. The relative stiffness differences between the INT and SIDE variants and REF change only slightly between the two meshes.

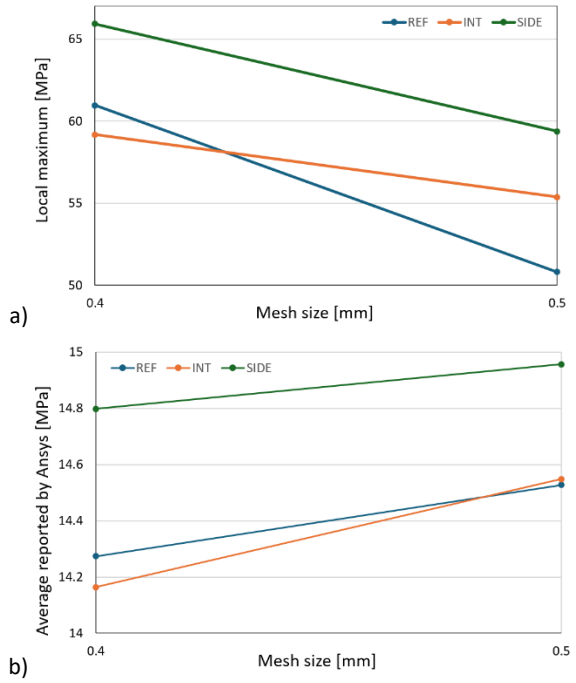



**Figure 5.** Effect of mesh size on the local maximum (a) and average stress (b) on the faces of the monitored strut

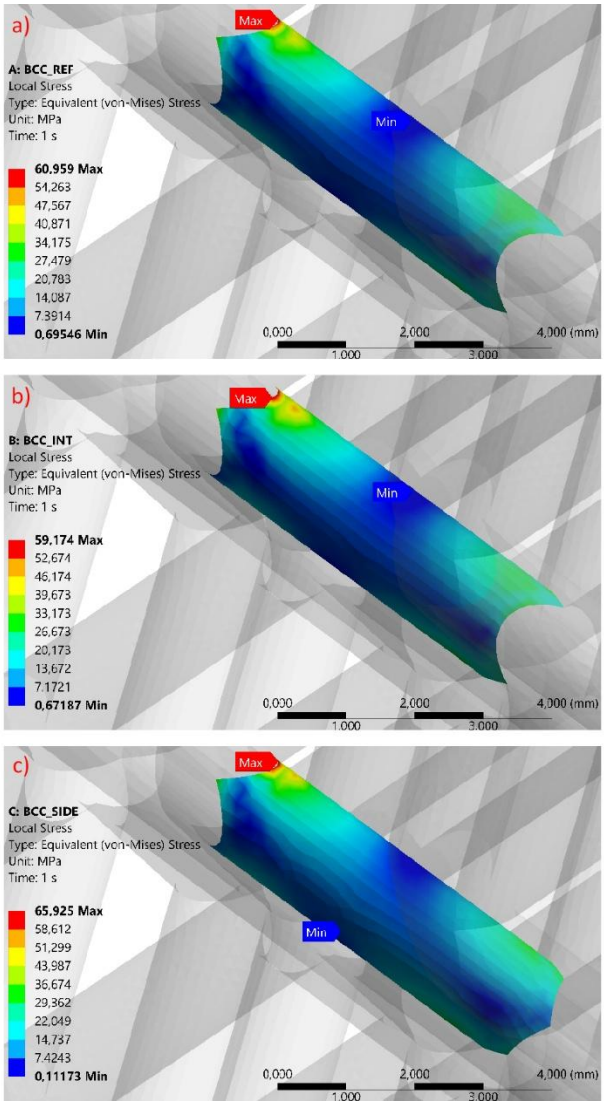



**Figure 6.** Distribution of von Mises equivalent stress on the surface of the monitored retained strut in the models at a mesh size of h = 0.4 mm – a) REF, b) INT, c) SIDE

Following mesh refinement, the local stress maxima increased by 19.97% for REF, by 6.85% for INT, and by 11.02% for SIDE. The Ansys-reported averages changed by −1.74%, −2.64%, and −1.06%. Within the range of mesh sizes examined, the local maximum is therefore more sensitive to element size than the reaction force or the reported average stress.

In the local stress maps, the stress maximum occurs at the joint at the end of the monitored strut. The local stress distribution is shown in Figure 6. The surfaces of the struts intersect in this region, and the result may depend strongly on the joint geometry, mesh, and stress averaging method. The two meshes used are insufficient to determine whether the maximum will stabilize or continue to increase with further refinement.

At h = 0.4 mm, the maximum von Mises equivalent stresses in the entire REF, INT, and SIDE specimens are 91.529 MPa, 93.968 MPa, and 91.377 MPa, respectively. For the SIDE specimen, the maximum on the monitored retained strut is 65.925 MPa. In this specimen, the overall maximum occurs at a joint with an end plate, outside the region of the missing strut. Figure 7 compares the stress distributions in the three specimens using a common color scale of 0–100 MPa. A missing strut can therefore alter the stress distribution in its vicinity even when the highest stress in the entire specimen occurs elsewhere.

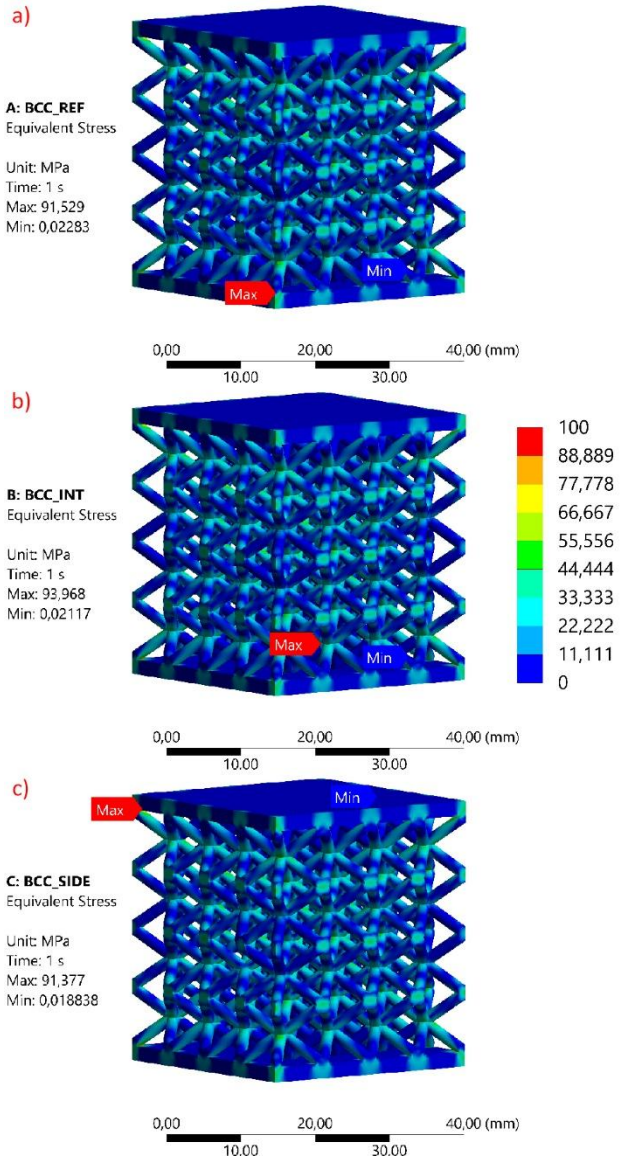



**Figure 7.** Distribution of von Mises equivalent stress on the surface of the entire specimen at a mesh size of h = 0.4 mm – a) REF, b) INT, c) SIDE

## 4 DISCUSSION

### 4.1 Evaluation of the results

The removal of one strut resulted in a small reduction in axial stiffness relative to the REF model in both variants. For INT, the reduction is approximately 0.593% for both meshes, while for SIDE it is approximately 0.276% to 0.282%. For the selected locations and the boundary conditions used, the internal defect therefore causes a greater reduction in the stiffness of the entire specimen than the lateral defect. This result applies to the specific models examined.

The stiffness differences between the variants are small, so it is also important to assess the effect of the mesh. Following refinement, the absolute stiffness values decreased by approximately 0.49% for all models. However, the stiffness ratios of INT and SIDE to their corresponding reference remain similar for both meshes. The comparison thus retains the same ranking of the variants. Nevertheless, results for two meshes are insufficient to determine the exact stiffness value under further refinement or fully quantify the numerical uncertainty of the small differences.

The reaction force describes the response of the entire specimen, while the local stress describes the stress state of a specific strut. Although SIDE has a smaller reduction in stiffness than INT, its maximum and reported average stress on the monitored strut are higher than those of REF for both meshes. The results at the same prescribed displacement suggest a redistribution of stress in this region. However, the magnitude of the increase in the local maximum depends on the mesh.

For INT, the local maximum is higher than that of REF for one mesh and lower for the other. These results therefore cannot reliably confirm the direction of the change in the maximum on the monitored strut. Its Ansys-reported average differs from the reference by less than 1%. The evaluation applies only to the selected strut, whose position relative to the internal and lateral defects differs. It therefore does not establish a general ranking of the severity of all internal and lateral defects.

The literature reports that the elastic behavior of lattice structures depends on the arrangement of the struts, their geometry, and defects [Gross 2019, Huang 2024]. The observed changes in stiffness and local stress are consistent with this finding. Direct numerical comparison with the cited studies is limited by differences in geometry, materials, loading, and the definition of defects. The present study compares three specific geometric variants using a common computational procedure.

### 4.2 Scope of applicability and limitations

The model uses the isotropic linear elastic properties of Structural Steel. These properties provide a common basis for comparing the three geometric variants, but they were not measured on a specific series of manufactured specimens. The calculations do not include surface roughness, internal pores, residual stresses, or manufacturing deviations in strut dimensions. Studies using the actual geometry demonstrate the importance of accounting for these deviations when modeling manufactured structures [Liu 2017, Lozanovski 2019, Bruson 2025].

The calculated stiffness applies to the specimen with the specified dimensions and end plates under the boundary restraints used. It includes plate deformation and the behavior of cells at the edges. One internal defect location and one lateral defect location are examined. Furthermore, removing one strut at different locations may not produce exactly the same reduction in material volume because this is affected by overlaps at the joints and trimming of the geometry at the specimen boundary. The observed stiffness differences therefore apply to these specific modifications of the geometry.

The detailed stress comparison is limited to selected surface faces of one retained strut. The “Average” value is used as the average reported by Ansys for this selection. The two mesh sizes allow the sensitivity of the results to be assessed, but do not confirm stabilization of the local stress maximum. The results represent the numerical response of an idealized geometry at the prescribed displacement. Their use in evaluating manufactured specimens would require experimental validation. The linear elastic analysis used cannot determine plastic collapse, fatigue life, or the energy absorbed during compression.

## 5 CONCLUSIONS

An intact BCC specimen, REF, was numerically compared with two variants containing one missing internal strut, INT, or one missing lateral strut, SIDE. All models had the same linear elastic material properties and a prescribed axial displacement of 0.01 mm. The results were compared at nominal element sizes of 0.5 and 0.4 mm.

Both defects reduced the axial stiffness of the entire specimen relative to REF. For INT, the reduction was approximately 0.593% for both meshes. For SIDE, it was 0.282% at a mesh size of 0.5 mm and 0.276% at a mesh size of 0.4 mm. At the selected defect locations, INT therefore exhibited a greater reduction in stiffness than SIDE. The stiffness ranking of REF, SIDE, and INT remained the same for both meshes.

Following mesh refinement, the axial stiffnesses of all three models decreased by approximately 0.49%. The local stress maxima were more sensitive to mesh size and increased by 6.85 to 19.97%. The Ansys-reported averages decreased by approximately 1.06 to 2.64%.

On the monitored strut, SIDE had a higher maximum and reported average stress than REF for both meshes. The local maximum was higher by 16.87% at a mesh size of 0.5 mm and by 8.15% at a mesh size of 0.4 mm. For INT, the maximum was higher than that of REF for one mesh and lower for the other, so the direction of its change cannot be reliably determined.

The results show that the reduction in the stiffness of the entire specimen and the change in stress on the selected strut describe different consequences of a missing strut. These quantities must therefore be assessed separately when evaluating a defect, and their sensitivity to the mesh must be taken into account. The conclusions apply to the geometry examined, the two specific defect locations, and the elastic loading used.


## ACKNOWLEDGMENTS

This work was supported by the Ministry of Education, Research, Development and Youth of the Slovak Republic under the VEGA grant No. 1/0119/26.


## REFERENCES


[Benedetti 2021] Benedetti, M., et al. Architected cellular materials: A review on their mechanical properties towards fatigue-tolerant design and fabrication. Materials Science and Engineering R: Reports, 2021, Vol. 144, 100606.

[Bozek 2023] Bozek, P., Krenicky, T., Prajova, V. Digital Induction Motor Model Based on the Finite Element Method. Applied Sciences, 2023, Vol. 13, No. 8, 5124. DOI: 10.3390/app13085124

[Bruson 2025] Bruson, D., et al. Revealing the (positive) role of porosity within polymeric additively manufactured lattices via X-ray computed tomography. International Journal of Solids and Structures, 2025, Vol. 320, 113488.

[Bulej 2022] Bulej, V., et al. Analysis of symmetrical/ asymmetrical loading influence of the full-suspension downhill bicycle's frame on the crack failure formation at a critical point during different driving scenarios and design improvement. Symmetry, 2022, Vol. 14, No. 2. DOI: 10.3390/sym140220255

[Dallago 2019] Dallago, M., et al. On the effect of geometrical imperfections and defects on the fatigue strength of cellular lattice structures additively manufactured via Selective Laser Melting. International Journal of Fatigue, 2019, Vol. 124, pp. 348–360.

[Dobrovszky 2024] Dobrovszky, P., et al. Impact of different TPMS tesselation approaches on mechanical properties of parts. MM Science Journal, 2024, No. June, pp. 7287–7293.

[Echeta 2020] Echeta, I., et al. Review of defects in lattice structures manufactured by powder bed fusion. The International Journal of Advanced Manufacturing Technology, 2020, Vol. 106, pp. 2649–2668.

[Goodall 2019] Goodall, R., et al. The Effects of Defects and Damage in the Mechanical Behavior of Ti6Al4V Lattices. Frontiers in Materials, 2019, Vol. 6, 117.

[Gross 2019] Gross, A., et al. Correlation between topology and elastic properties of imperfect truss-lattice materials. Journal of the Mechanics and Physics of Solids, 2019, Vol. 124, pp. 577–598.

[Gumruk 2013] Gümrük, R. and Mines, R.A.W. Compressive behaviour of stainless steel micro-lattice structures. International Journal of Mechanical Sciences, 2013, Vol. 68, pp. 125–139.

[Hanks 2020] Hanks, B., et al. Mechanical properties of additively manufactured metal lattice structures: Data review and design interface. Additive Manufacturing, 2020, Vol. 35, 101301.

[Huang 2024] Huang, Z., et al. Numerical and experimental evaluations on the defect sensitivity of the performance of BCC truss-lattice structures. Mechanics of Materials, 2024, Vol. 191, 104937.

[Liu 2017] Liu, L., et al. Elastic and failure response of imperfect three-dimensional metallic lattices: the role of geometric defects induced by Selective Laser Melting. Journal of the Mechanics and Physics of Solids, 2017, Vol. 107, pp. 160–184.

[Lozanovski 2019] Lozanovski, B., et al. Computational modelling of strut defects in SLM manufactured lattice structures. Materials & Design, 2019, Vol. 171, 107671.

[Maconachie 2019] Maconachie, T., et al. SLM lattice structures: Properties, performance, applications and challenges. Materials & Design, 2019, Vol. 183, 108137.

[Safka 2020] Safka, J., et al. Mechanical properties of two types of lattice structures fabricated with the use of HP MultiJet Fusion technology. MM Science Journal, 2020, November, pp. 4074–4079.

[Saga 2018] Saga, M., Vasko, M., Sagova, Z., Handrik, M. Effective algorithm for structural optimization subjected to fatigue damage and random excitation. Scientific Journal of Silesian University of Technology-Series Transport, 2018, Vol. 99. DOI: 10.20858/sjsutst.2018.99.14, 2018

[Tkac 2020] Tkac, J., et al. Analysis of mechanical properties of a lattice structure produced with the additive technology. Composite Structures, 2020, Vol. 242, 112138.

[Tkac 2022] Tkac, J., et al. Possibilities of analysis of porous structures using industrial computed tomography. Engineering Failure Analysis, 2022, Vol. 137, 106296.

[Ushijima 2011] Ushijima, K., et al. An investigation into the compressive properties of stainless steel micro-lattice structures. Journal of Sandwich Structures & Materials, 2011, Vol. 13, No. 3, pp. 303–329.

[Vrana 2020] Vrana, R., et al. Shape and dimensional analysis of lattice structures produced by selective laser melting. MM Science Journal, 2020, No. June, pp. 3938–3942.

**CONTACTS:**

**Ing. Jozef Tkac, PhD.**
Technical University of Kosice
Faculty of Manufacturing Technologies with a seat in Presov
Department of Computer Aided Manufacturing Technologies
Sturova 31, Presov, 080 01, Slovak Republic
+421 55 602 6364, jozef.tkac@tuke.sk, https://kppvt.fvt.tuke.sk/katedra/pracovnici/tkac-en/

**LICENSE CREATIVE COMMONS:**

The article is published under the terms and conditions of the Creative Commons Attribution 4.0 International License (CC BY 4.0).